Precise Aspiration and Positioning Control based on Dynamic Model *inside* and *outside* the Micropipette

Mingzhu Sun, Yatong Yao, Xiangfei Zhao, Lu Li, Huiying Gong, Jinyu Qiu, Yaowei Liu, Xin Zhao*

***Abstract*—Cell aspiration is a common technique in cell manipulation for cell transfer or intracellular property measurement. In this paper, we present a robotic micromanipulation system for cell aspiration and positioning by a micropipette. Considering the relative motion of the object and the fluid, we first establish an overall dynamic model of microbead motion inside and outside the micropipette based on computational fluid dynamics (CFD). Then we design an adaptive sliding mode controller (ASMC) for microbead aspiration outside the micropipette and positioning inside the pipette based on the dynamic model. The controller is proven to achieve asymptotic stability by Lyapunov techniques. Simulation and experimental results demonstrate the effectiveness of the fluid model and the performance of the designed control system.**

***Note to Practitioners*—Cell aspiration with a micropipette is a key technology in cell manipulation. Generally, there is relative motion between the aspirated object and the fluid, resulting in large overshoot even aspiration failure. In this paper, we set up an overall dynamic model of microbead motion inside and outside the micropipette, combining microbead motion dynamics, fluid dynamics and pneumatic pump modeling. Based on this model, we design an ASMC for microbead aspiration outside the micropipette and positioning inside the pipette. In simulations and experiments, the positioning errors of the microbead of different sizes converge to zero without overshoot, revealing the strong robustness of the controller. Applications for this technology include cell or sperm aspiration and injection.**

***Index Terms*—micromanipulation system, cell aspiration control, fluid modeling, adaptive sliding mode control.**

I. Introduction

CELL aspiration with a micropipette is widely used in cell manipulation for cell transfer or intracellular property measurement [1], [2]. Normally, the tip of the micropipette approaches a target cell, and the pump connected to the micropipette produces negative pressure by changing the piston position of the pump. Then the cell medium around the pipette flows, generating a draw force on the cell. The target cell is aspirated into the pipette and move to the desired position inside the pipette finally.

In bio-medical experiments, the diameter of the micropipette tip ranges from a few microns to one hundred microns according to the sizes of the aspirated cells. When the cell medium flows into the micropipette, the fluid velocity will increase rapidly due to the small size of the pipette tip. In manual operation, the pump is controlled by the operators. It usually takes less than one second for the cell to reach the target position from cell movement. The cell would pass through the desired position at a high speed, even disappear in the microscopic field of view because of the large overshoot. The operator needs to adjust the pump repeatedly to make the cell return to the desired position, which increases the system uncertainty and operating time.

Recently, a number of approaches have been reported in the literature for aspiration and positioning of single cell [3], [4], [5], [6], [7], [8]. As for aspiration and positioning control, a robotic manipulation system for living cell selection and transfer was presented based on vision-based feedback and closed-loop process control [9]. A volume of medium and the target cell was aspirated into the pipette. The cell could be successfully aspirated, but it would disappear into the micropipette since the aspiration process was not well controlled. A closed-loop robust controller integrating cell dynamics was designed to position the cell inside the micropipette [10]. Human sperm cells were used as the controlled objects in experimentation. Since the head width of the sperm is only $3\mu m$, it was assumed that there was no relative motion between the sperm and the culture medium, which is not applicable to most kinds of cells. As for the larger cells, a linear quadratic regulator (LQR) controller was developed to aspirate the embryo with about $100\mu m$ in diameter [11]. This controller could perform multi-embryo aspiration with a minimum volume of the excess medium. Subsequently, a nonlinear dynamic model of cell motion inside the pipette was established by considering oil compressibility and connecting tube's deformation. Based on this model, an adaptive controller was designed to aspirate and control the position of the cell inside the micropipette accurately [12]. This method could be applied to the cells of different sizes, but the system exhibited overshoot with the decrease of the cell size. Specifically, the smaller the cell size, the larger the overshoot.

When a microbead, for example, the cell, moves with the fluid, there is relative motion between the bead and the fluid. The microbead is subjected to the draw force, which is positively related to the relative velocity between the bead and the fluid [13]. When the liquid enters the pipette from the outside, the sudden change of the fluid velocity will lead to the sudden increase of the draw force on the microbead, as well as the acceleration of the microbead movement. As the size of the microbead decreases, the tip of the aspiration pipette becomes thinner, and the draw force is bigger. Meanwhile, the mass of

This research was jointly supported by National Key R&D Program of China (2018YFB1304905), National Natural Science Foundation of China (62027812, U1813210, 62003174, 61903201) and China Postdoctoral Science Foundation (2020M680865).

Authors are with the Institute of Robotics and Automatic Information System (IRAIS) and the Tianjin Key Laboratory of Intelligent Robotic (tjKLIR), Nankai University, Tianjin 300350, China, and Institute of Intelligence Technology and Robotic Systems, Shenzhen Research Institute of Nankai University, Shenzhen 518083, China.

*Contacting Author: Xin Zhao. (e-mail: zhaoxin@nankai.edu.cn)

the microbead becomes smaller, which makes the microbead produce a greater acceleration, increasing the control greatly difficulty. The existing methods usually started the control process of cell movement after the cell being aspirated into the pipette. Therefore, it is difficult to avoid overshoot when small beads enter the pipette at high initial acceleration.

In this paper, we establish an overall dynamic model of microbead motion inside and outside the micropipette, and control the whole aspiration process. The dynamic model includes dynamics of microbead motion, fluid dynamics and pneumatic pump modeling, where the difficulty lies in fluid modeling. The existing methods assumed that there was no relative motion between the cell and liquid inside the pipette, since the cell motion is confined by the pipette wall [11]. So, the change of the fluid volume was described by cell motion, which is obviously untenable outside the pipette.

Generally, the physical behavior of fluid flow is governed by three fundamental principles. The transport equations to solve flow problems are partial differential equations (PDE), which are known as the Navier–Stokes equations for isothermal systems [14]. It is of great difficulty to get the analytical solutions of these PDEs, so as to design the controller. Computational fluid dynamics (CFD) solves the transport equations by numerical analysis [15]. It is widely employed in the simulation and analysis of fluid mechanics problems, e.g., energy separation mechanism investigation [16], [17], and indoor temperature prediction [18], [19]. The numerical simulations obtained results within good agreement with the experimental studies.

In this paper, CFD is applied to connect the fluid flow driven by the pump to the microbead motion, forming an overall dynamic model inside and outside the micropipette. The model includes the characteristics of the microbead, fluid, micropipette, pneumatic pump and stepper motor. Subsequently, an adaptive sliding mode controller (ASMC) is proposed, which achieves asymptotic stability and fast convergence in the presence of various parameter uncertainties [20]. Finally, simulations and experiments of the polystyrene microbeads of different sizes are performed to verify the performance of the designed control system.

Compared with the existing works, the contributions of this paper are summarized as follows:

1) We set up an overall dynamic model of microbead motion by combining microbead motion dynamics, fluid dynamics and pneumatic pump modeling. The velocity filed inside and outside the micropipette is calculated based on CFD by using finite element simulation software ANSYS Fluent. The model presents high precision and provides a solid foundation for system analysis and controller design.
2) We design an adaptive sliding mode controller to control the aspiration and positioning of the microbead precisely even when the parameters within the system are unknown. Simulation and experimental results demonstrate the performance of the designed control system.

The rest of the paper is organized as follows. Section II provides an overall dynamic model of microbead aspiration and positioning, and formulates the control problem. The controller design and the rigorous stability analysis are given in Sections III. In Section IV, the model is validated first, and then, simulation and experimental tests are performed to verify the performance of the system. At last, the paper is concluded in Section VI.

II. Modeling

A. Overall dynamic model

The aspiration and positioning system is shown in Fig. 1, the origin of the system is set to the center of the micropipette tip. The micropipette is placed horizontally in the liquid along X-axis. The pneumatic pump, connecting tube and the micropipette with liquid at the tip form a closed gas space. As the piston moves, the change of gas pressure leads to the fluid flow inside and outside the micropipette. Then, the flow of the fluid exerts draw force on the microbead and makes it move.

Normally, the micropipette is moved to its initial position before aspiration, where the pipette tip is close to the bead and the pipette center is aligned with the bead, as shown in Fig. 1. The bead will move along the micropipette (X-axis) in the center of the pipette after being aspirated into the pipette, so we use the horizontal position x of the microbead instead of its 3D position $(x, 0, 0)$ for simplicity.

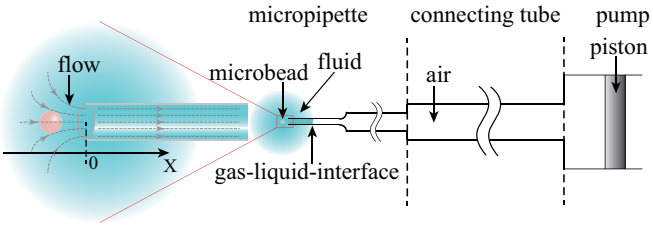

Fig. 1. The aspiration and positioning system. The system consists of the pneumatic pump, connecting tube and the micropipette.

It is difficult to directly deduce the relationship between the piston motion and the fluid flow at the position of the microbead. To be noted that the gas pressure change caused by the piston motion will make the gas-liquid-interface (GLI) move. As the boundary of fluid in the micropipette, the motion of GLI must be related to the fluid flow at the position of the microbead. Therefore, GLI is utilized as a medium to establish the relationship between piston motion and fluid flow. As shown in Fig. 2, there are three parts in the overall model of the aspiration and positioning system:

(1) The dynamic model of the microbead in fluid.
(2) The fluid model based on GLI.
(3) The pneumatic pump model oriented to GLI.

When the microbead moves in fluid, it is mainly affected by the draw force produced by the fluid. Since the pipette center is aligned with the bead, the draw force on the microbead is along X-axis, as shown in Fig. 3. The dynamic equation is:

$$m\ddot{x} = F_d \tag{1}$$

where m and x are the mass and the horizontal position of the microbead respectively. F_d is the draw force on the bead.

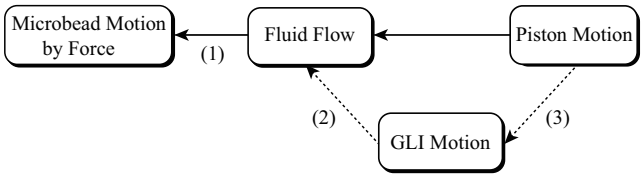

Fig. 2. The overall model of the aspiration and positioning system.

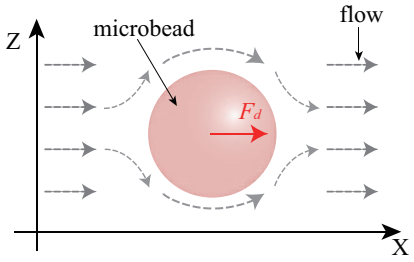

Fig. 3. The dynamic model of the microbead in fluid.

According to Stokes' Law, the draw force can be calculated at low Reynolds number [13]:

$$F_d = 6\pi\mu r\left(v_f(x) - \dot{x}\right) \tag{2}$$

where r is the radius of the microbead, μ is the dynamic viscosity of the fluid, $v_f(x)$ is the fluid velocity along X-axis at the position of the microbead. Eq. (2) is applicable to both the inside of the micropipette and the open environment near the pipette tip.

For viscous incompressible fluid, Navier Stokes equations are applied to describe the motion of the fluid:

$$\rho\left(\frac{\partial \mathbf{V}}{\partial t} + (\mathbf{V}\cdot\nabla)\mathbf{V}\right) = -\nabla p + \mu\nabla^2\mathbf{V} + \mathbf{F} \tag{3}$$

where $\mathbf{V} = (v_x, v_y, v_z) \in \mathbf{R}^3$ is the velocity vector of the fluid unit. $\mathbf{F}$ is the external force exerted on the fluid unit. ∇p is the pressure gradient in the fluid. Constants ρ and μ are the density and the dynamic viscosity of the fluid.

Eq. (3) describes the motion of the fluid. In the aspiration and positioning system, the fluid velocity vector at GLI $\mathbf{V}_{\mathrm{GLI}}$ is the boundary condition of the above PDEs. If the equations could be solved, the relationship between the fluid velocity at GLI $\mathbf{V}_{\mathrm{GLI}}$ and the fluid velocity at the position of the microbead $v_f(x)$ would be obtained. The relationship has the following form:

$$v_f(x) = h\left(x, \mathbf{V}_{\mathrm{GLI}}\right) \tag{4}$$

According to Boyle's Law, we have:

$$P_0V_0 = P'V' \tag{5}$$

where P_0 and P' are the pressures in two consecutive moments, V_0 and V' are the corresponding volumes of the gas.

For the closed gas in the system, let P_0 and V_0 be the initial pressure and volume of the gas, respectively. When the piston of the pneumatic pump moves backward with distance Δl_1, let that the change of gas pressure is Δp, and GLI moves in the opposite direction of the pipette tip with distance Δl_2. Omitting the change of the cross-sectional area at GLI, the changed pressure P' and volume V' are expressed as:

$$\begin{aligned} P' &= P_0 - \Delta p \\ V' &= V_0 - A_2\Delta l_2 + A_1\Delta l_1 \end{aligned} \tag{6}$$

where A_1 is the sectional area of the piston, A_2 is the sectional area at GLI.

Combining Eqs. (5) and (6), we have:

$$\Delta l_2 = \frac{A_1}{A_2}\Delta l_1 - \frac{V_0}{A_2P_0}\Delta p + \frac{1}{P_0}\Delta p\Delta l_2 - \frac{A_1}{A_2P_0}\Delta p\Delta l_1 \tag{7}$$

Omitting the third and fourth higher-order infinitesimal items on the right side of Eq. (7), and dividing both sides by time interval Δt, we have:

$$v_{\mathrm{GLI}} = \frac{A_1}{A_2}\frac{\Delta l_1}{\Delta t} - \frac{V_0}{A_2P_0}\dot{p} \tag{8}$$

where v_{GLI} is the velocity of GLI. we set $v_{\mathrm{GLI}} = \max\left(\mathbf{V}_{\mathrm{GLI}}\right)$. $\dot{p}$ is the change rate of the gas pressure in the pneumatic pump. The pump is driven by a stepper motor, so we have:

$$\Delta l_1 = \frac{k_\theta S\Delta n_m}{2\pi} \tag{9}$$

where k_θ and S represent the step angle and the lead of stepper motor's shaft, respectively. Δn_m is the number of pulses sent to the stepper motor.

Summing up Eqs. (8) and (9), we obtain:

$$v_{\mathrm{GLI}} = \frac{A_1}{A_2}\frac{k_\theta S}{2\pi}v_m - \frac{V_0}{A_2P_0}\dot{p} \tag{10}$$

where $v_m = \Delta n_m/\Delta t$ is the pulse frequency sent by the host computer.

B. Fluid velocity modeling based on CFD

In the dynamic model of the aspiration and positioning system, all the equations are analytic except Eq. (4). Theoretically, fluid flow can be determined by solving Navier Stokes equations of Eq. (4) with some initial conditions and boundary conditions. However, it is difficult to find the exact solution of the equations due to the viscous effect. In this paper, we assume that the microbead does not affect the velocity distribution in the space and analyze the relationship between the fluid velocity and the velocity of GLI by CFD software ANSYS. The geometric model of micropipette aspiration is designed by using ANSYS DesignModeler, as shown in Fig. 4(a). The distribution of fluid velocity field is solved numerically by using ANSYS FLUENT. We use the K-omega turbulence model in simulation and set the boundary condition of the inlet as pressure.

For the commonly used micropipette with $20\mu m$ inner diameter and $25\mu m$ outer diameter, the distribution of fluid velocity field is shown as Fig. 4(b). In the micropipette, fluid motion is smooth and constant, which is a typical laminar flow. Outside the micropipette, the fluid velocity decreases rapidly, the velocity is almost zero at $50\mu m$ outside the micropipette

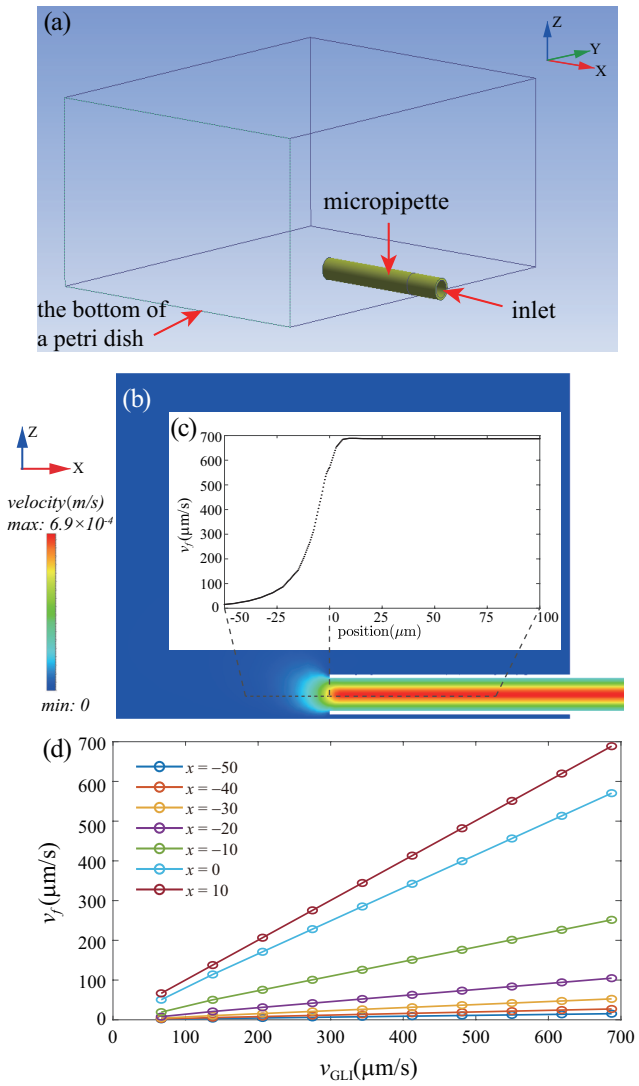

Fig. 4. (a) Geometric model of micropipette aspiration. (b)-(c) Simulation results of fluid velocity distribution. (d) Relationship between the fluid velocity at different locations and that at the center of GLI.

tip. Fig. 4(c) shows the fluid velocity $v_f(x)$ from -50μm to 100μm along X-axis. Outside the pipette, the fluid velocity increases, as the fluid approaches the pipette tip. When the fluid flows into the pipette, the fluid motion tends towards stability, the steady velocity equals to the fluid velocity at the center of GLI v_{center}.

According to Eq. (4), the fluid velocity $v_f(x)$ is related to the horizontal position x and the fluid velocity at the center of GLI v_{center}. Ten groups of simulations with different inlet pressures were performed to determine the relationship. Fig. 4(c) shows the relationship between the fluid velocity $v_f(x)$ and fluid velocity at the center of GLI v_{center}. We analyze 7 different locations near the pipette tip ranging from -50μm to 10μm along X-axis, each line in Fig. 4(c) represents a horizontal position. The simulation results indicate that $v_f(x)$ at the same horizontal location is linear with v_{center} with different inlet pressures. Therefore, Eq. (4) can be rewritten as follows:

$$v_f(x) = h(x)v_{\text{center}} \tag{11}$$

TABLE I
THE FITTING RESULTS OF THE PROPORTION FUNCTION $h(x)$

NO.	Inner diameter(μm)	Inclination angle(°)	α	β	R^2
1	10	0	29.45	2.459	0.9996
2		5			0.9995
3	15	0	78	4.162	0.9987
4		5			0.9982
5	20	0	139.1	5.454	0.9985
6		5			0.9986
7	30	0	314.3	8.096	0.9980
8		5			0.9980
9	40	0	486.8	9.955	0.9981
10		5			0.9982
11	60	0	1177	15.52	0.9977
12		5			0.9981
13	80	0	1833	31.98	0.9991
14		5			0.9979
15	100	0	3120	39.56	0.9988
16		5			0.9981
17	120	0	4490	49.33	0.9983
18		5			0.9905

In laminar flow, the flow velocity in the center of the micropipette is the highest, which means $v_{\text{center}} = \max(\mathbf{V}_{\text{GLI}}) = v_{\text{GLI}}$, so we have:

$$v_f(x) = h(x)v_{\text{GLI}} \tag{12}$$

where v_{GLI} is the velocity of GLI defined in Eq. (10).

We further establish the relationship between the position x and proportion function $h(x)$. The data in Fig. 4(b)(ii) is analyzed by nonlinear regression. We select the following expected function, which is continuous and differentiable:

$$h(x) = \frac{v_f(x)}{v_{\text{GLI}}} = \begin{cases} \frac{\alpha}{(x-\beta)^2+\alpha} & , x < \beta \\ 1 & , x \geq \beta \end{cases} \tag{13}$$

The fitting results are $\alpha = 139.1$, $\beta = 5.454$ for the micropipette with 20μm inner diameter. The goodness of fit is greater than 0.99.

In aspiration experiments, the diameter of the micropipette varies due to the size of the microbead, and the pipette cannot be assembled exactly horizontally. Therefore, we carry out 18 groups of simulations with different pipette diameters (10, 15, 20, 30, 40, 60, 80, 100, 120μm) and inclination angles (0°, 5°) to extend the model to the general case. Table 1 shows the fitting results of Eq. (13). All the goodness of fit is greater than 0.99, indicating the great adaptability of the model.

As shown in Table 1, the inner diameter of the micropipette has a significant effect on the fitting parameters α and β in Eq. (13). We analyze the relationship between the inner diameter and α/β by exponential fitting. Fig. 5 and Eq. (14) show the fitting results:

$$\begin{aligned} \alpha &= 0.27d^{2.03} \quad for \quad d \in [10, 120] \quad R^2 = 0.9986 \\ \beta &= 0.13d^{1.24} \quad for \quad d \in [10, 120] \quad R^2 = 0.9831 \end{aligned} \tag{14}$$

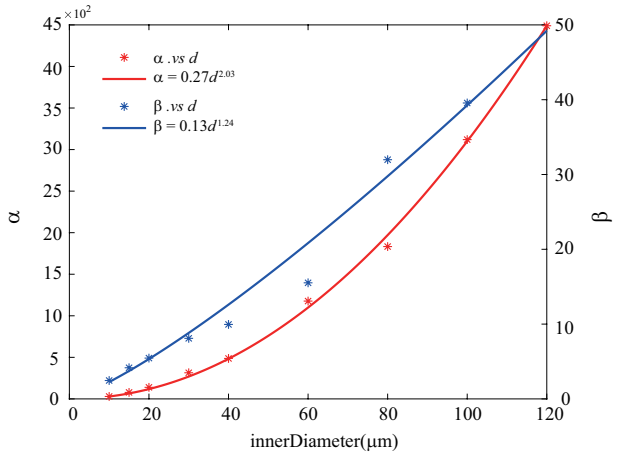

Fig. 5. The fitting results of α and β in Eq. (11) and the inner diameter of the pipette.

where d is the inner diameter of the pipette. We further perform transient simulations to analyze the dynamic performance of the proportion function $h(\cdot)$. The simulation results reveal that Eq. (13) of $h(\cdot)$ still holds with high-frequency input. See **Appendix A** for more detail.

In summary, the dynamic model of the aspiration and positioning system under external disturbance can be deduced by combining Eqs. (1), (2), (10), (12):

$$\ddot{x} = -\frac{6\pi\mu r}{m}\dot{x} + \frac{3\mu r A_1 k_\theta S}{A_2 m}h(x)u - \frac{6\pi\mu r V_0}{A_2 P_0 m}h(x)\dot{P} + \omega \quad (15)$$

$$h(x) = \begin{cases} \frac{0.27d^{2.03}}{(x-0.13d^{1.24})^2+0.27d^{2.03}} & , x_{min} \le x < 0.13d^{1.24} \\ 1 & , x \ge 0.13d^{1.24} \end{cases} \quad (16)$$

where, u, which represents the pulse frequency sent by the host computer, is the control variable of the system. ω represents the system disturbance. x_{min} is the minimum value of the cell position, which is -50μm. $d \in [10, 120]\mu m$ is the inner diameter of the micropipette.

III. Controller Design

A. Adaptive sliding mode controller design

In the aspiration and positioning system, some parameters in the system dynamics, including the mass of the microbead m, the dynamic viscosity of the fluid, the initial volume V_0 and the initial pressure P_0 of the gas, cannot be measured accurately in the experiment. Meanwhile, the positioning process is affected by external disturbances inevitably. Therefore, we design an adaptive sliding mode controller in this paper to make the microbead locate to the desired position in the pipette steady and rapidly. Fig. 6 shows the control architecture of the system. The target bead is observed through the microscope and CCD camera, its position is detected based on the image processing method and used as the visual feedback of the controller.

Let $a_0 = \frac{6\pi\mu r}{m}$, $b_0 = \frac{3\mu r A_1 k_\theta S}{A_2 m}$, Eq. (15) can be rewritten as:

$$\ddot{x} = -a_0\dot{x} + b_0 h(x)u + d(t) \quad (17)$$

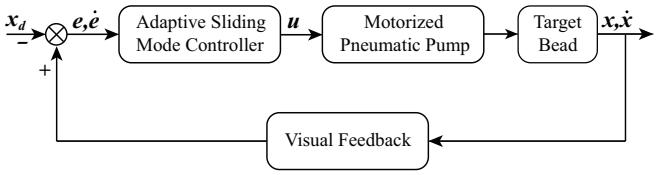

Fig. 6. Control architecture of the aspiration and positioning system.

where $d(t) = -\frac{6\pi\mu r V_0}{A_2 P_0 m}h(x)\dot{P} + \omega$, represents the time-varying resultant disturbance. Note that $d(t)$ is a function of both the unknown internal dynamics and the external disturbance.

To facilitate the following description, the disturbance is redefined as $\tilde{d}(t) = \frac{d(t)}{b_0}$.

Assumption 1: It is assumed that the disturbance is uniformly bounded, i.e., $|\tilde{d}(t)| \le \delta$.

Define the tracking error as:

$$e \triangleq x - x_d \quad (18)$$

where x_d is the desired position in the micropipette. Set the sliding surface as [21]:

$$s = ce + \dot{e} \quad (19)$$

where c is a controller parameter to be designed and $c > 0$.

Define the unknown parameters as $\theta_1 \triangleq \frac{a_0}{b_0}$, $\theta_2 \triangleq \frac{1}{b_0}$ and design the control law as:

$$u = \frac{1}{h(x)}\left(-ks + \hat{\theta}_1\dot{x} - \hat{\theta}_2\left(c\dot{e} - \ddot{x}_d\right) - \hat{\delta}\tanh(s)\right) \quad (20)$$

where $tanh(\cdot)$ denotes the hyperbolic tangent function, which can suppress the chattering phenomena obviously in sliding mode control. k is a positive control gain. $\hat{\delta}$, $\hat{\theta}_1$, $\hat{\theta}_2$ are the estimations of δ, θ_1, θ_2, respectively, which are generated by the following update laws:

$$\begin{aligned} \dot{\hat{\theta}}_1 &= -\gamma_1\dot{x}s \\ \dot{\hat{\theta}}_2 &= \gamma_2\left(c\dot{e} - \ddot{x}_d\right)s \\ \dot{\hat{\delta}} &= \lambda|s| \end{aligned} \quad (21)$$

where γ_1, γ_2, λ are positive update gains.

B. Stability analysis

Proof: The Lyapunov technique is utilized to prove the stability of the designed control system. Define the following Lyapunov function candidate:

$$V = \frac{1}{2b_0}s^2 + \frac{1}{2\gamma_1}(\hat{\theta}_1 - \theta_1)^2 + \frac{1}{2\gamma_2}(\hat{\theta}_2 - \theta_2)^2 + \frac{1}{2\lambda}(\hat{\delta} - \delta)^2 \quad (22)$$

The time derivative of Eq. (22) can be expressed as:

$$
\begin{aligned}
\dot{V} =& \frac{1}{b_0} s(c\dot{e} + \ddot{e}) + \frac{1}{\gamma_1}(\hat{\theta}_1 - \theta_1)\dot{\hat{\theta}}_1 \\
&+ \frac{1}{\gamma_2}(\hat{\theta}_2 - \theta_2)\dot{\hat{\theta}}_2 + \frac{1}{\lambda}(\hat{\delta} - \delta)\dot{\hat{\delta}} \\
=& \frac{s}{b_0}(c\dot{e} - a_0\dot{x} + b_0 h(x)u + d(t) - \dot{x}_d) \\
&- (\hat{\theta}_1 - \theta_1)\dot{x}s + (\hat{\theta}_2 - \theta_2)\left(\dot{e} - \ddot{x}_d\right)s + (\hat{\delta} - \delta)|s| \\
=& s[-\theta_1\dot{x} + \theta_2\left(c\dot{e} - \ddot{x}_d\right) - ks - \hat{\delta}\tanh(s) \\
&+ \hat{\theta}_1\dot{x} - \hat{\theta}_2\left(c\dot{e} - x'\alpha\right) + \frac{d(t)}{b_0}] \\
&- (\hat{\theta}_1 - \theta_1)\dot{x}s + (\hat{\theta}_2 - \theta_2)(c\dot{e} - \dot{x}_d)s + (\hat{\delta} - \delta)|s| \\
=& -ks^2 - \hat{\delta}\tan h(s)s + \frac{d(t)}{b_0}s + (\hat{\delta} - \delta)|s| \\
\leqslant& -ks^2 - \hat{\delta}|s| + \delta s + (\hat{\delta} - \delta)|s| \\
\leqslant& -ks^2 + \delta s - \delta|s| \\
\leqslant& -ks^2
\end{aligned}
\tag{23}
$$

implying that V is bounded by the initial value. Based on Eqs. (15), (18) and (19), the conclusion can be derived as follows by using the LaSalle-Yoshizawa theorem [22]:

$$
s \to 0 \text{ as } t \to \infty \Rightarrow e \to 0 \text{ as } t \to \infty \tag{24}
$$

namely, the tracking error e converges to zero and the system is asymptotically stable.

IV. Simulation and Experiments

A. System setup

The proposed aspiration and positioning system, as shown in Fig. 7, is integrated based on an inverted microscope (Ti-E, Nikon) with a $10\times$ or $20\times$ objective. A motorized X-Y stage (ProScan III, Prior, motion range: $120mm \times 80mm$, positioning resolution: $0.05\mu m$) is used to hold the petri dish containing culture medium and microbeads, which are manipulated by the micropipette. The micropipette is connected to a motorized pneumatic pump through connecting tubes and the micropipette holder (HI-7, Narishige, Japan). The micropipette holder is mounted on two 3-DOF motorized X-Y-Z micromanipulators (MP285, Sutter, motion range: $25mm$, positioning resolution: $0.04\mu m$). A CCD camera (acA645-100gm, Basler) is mounted on the microscope for visual feedback. All components are fixed on a vibration isolation table. The control algorithm is programmed using C++.

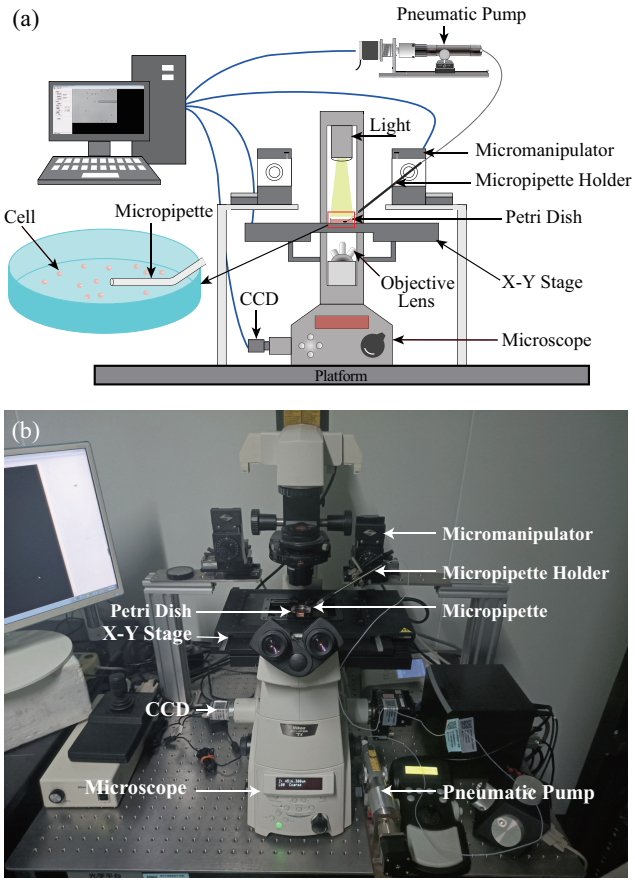

Fig. 7. System setup.

B. Model validation

The proposed fluid model describes the fluid velocity field inside and outside the micropipette. We design a particle aspiration experiment to verify this model. In fluid mechanics, a streamline is defined as a line that is everywhere tangent to the velocity field [23]. To visualize the streamline in a flow, we should imagine the motion of the particles suspended in the fluid and carried along with it, which is very difficult in the experiments. A pathline is a trajectory traced by the single fluid particle during the flow, which gives a traveling history of the fluid element over a specified time interval. In steady flow, streamline and pathline coincide. Therefore, we use the pathline instead of the streamline to analyze the velocity distribution.

The polystyrene particles with $1\mu m$ diameter are utilized for model validation. It is assumed that there is no relative motion between the particles and the liquid due to the small size of the particles. In the experiment, plenty of the polystyrene particles are suspended in the liquid and aspirated by the pump with a constant speed of the piston. The motion of the particles is recorded by the high-speed camera (C110, PHANTOM). We choose the particle located in the center of the pipette and track it by using an optical flow algorithm. Fig. 8 shows the visual tracking results of the key locations, as well as the normalized fluid velocity distribution along X-axis after mean filtering. Eq. (13) is used for data fitting, as shown in the red line of Fig. 8. The mean square error is 0.0329, indicating the effectiveness of the fluid model.

C. Simulations

Simulations are performed to verify the performance of the proposed controller before applying it to the actual system. The model and the controller are built in Matlab/Simulink. The model parameters are set as $m = 1mg$, $r = 8\mu m$, $\mu = 1656.9 \times 10^{-18}\mu m^2/s$, $A_1 = 500\mu m$, $A_2 = 20\mu m$, $k_\theta = 0.0281°$, and $S = 50\mu m$. The control gains are chosen as

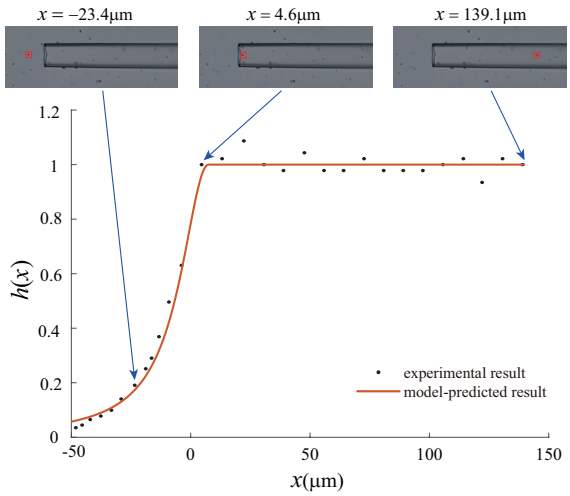

Fig. 8. The measurement and the model prediction results of the fluid velocities.

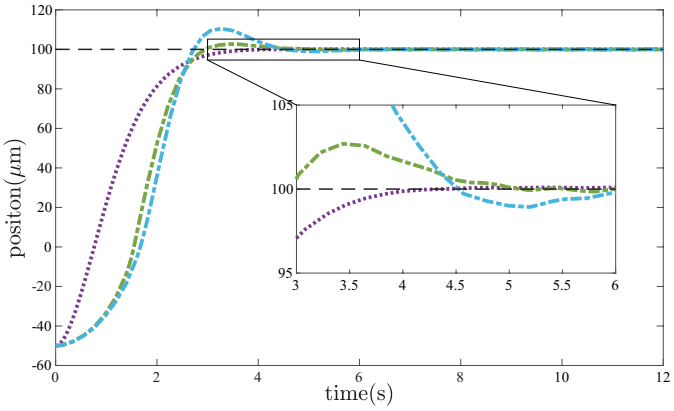

Fig. 9. Simulation results. (grey dashed—desired position; purple line—proposed method; green line—adaptive controller; blue line—PD controller)

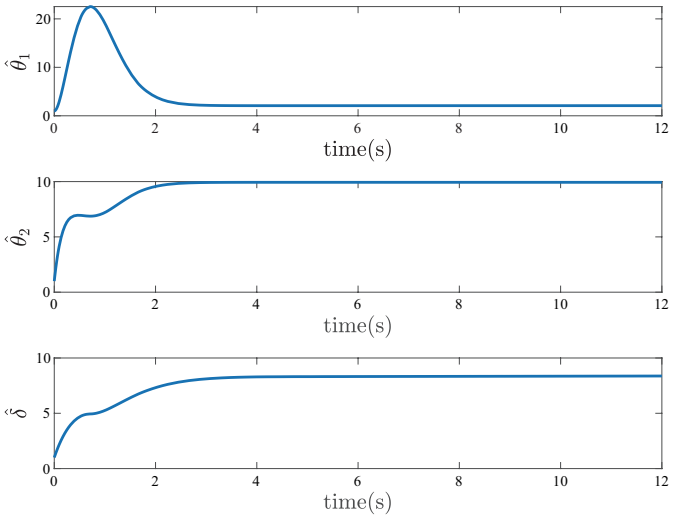

Fig. 10. Parameter estimation.

$k = 100$, and $c = 0.9$. The proposed ASMC parameters of update law are set as $\gamma_1 = 0.012$, $\gamma_2 = 0.001$, $\lambda = 0.1$.

The proposed controller is compared with the model-based adaptive controller [12] and PD controller. In adaptive control, the microbead is aspirated by the pump at a constant speed of the piston outside the pipette, and controlled inside the pipette. In PD control, the PD parameters are optimized and set as $k_p = 200$ and $k_d = 100$. The initial position and the desired position of the microbead are set to -50 and $100\mu m$, the external disturbance is modeled as $10\sin(10t)$.

Fig. 9 shows the simulation results, where the grey dashed line denotes the desired position, the purple line, the green line, and the blue line represent the microbead trajectories under the proposed ASMC, the adaptive controller and the PD controller, respectively. The proposed ASMC converges to the desired position faster than the adaptive controller and the PD controller without overshoot. Fig. 10 shows the parameter update process. In the time interval [0s, 3s], the unknown parameters are estimated and adjusted online to improve the control performance of the system. The update process stops until the actual position of the microbead converges to the desired value asymptotically.

D. Experiments

In order to further verify the effectiveness and superiority of the proposed micropipette aspiration and positioning control method, the actual implementation and testing are adopted in the system shown in Fig. 7, and compared with the traditional control methods.

The differences between individual cells and the changes in cell properties caused by long-term experiments will introduce additional effects to comparative experiments. Therefore, the polystyrene microbeads with the same size as the cells, with less individual variability, and better stability are used as experimental objects.

1) Visual Feedback: The images of the micropipette do not change during the operation, so template matching is used to detect and locate the micropipette tip. Set the detected position of the micropipette tip as (xtip; ytip), the region containing the whole micropipette is selected as the region of interest (ROI) for microbead tracking (Fig. 11(a)). Since the light intensity is stable and the position of the micropipette does not change, the background subtraction method is used to track the microbead of interest. Fig. 11(a) and (b) show the background image captured before the microbeads move and the current image captured in real time during the process of micropipette aspiration and positioning. The difference image is then binarized by OTSU adaptive threshold method and denoised by morphological closing operation (Fig. 11(c)). The microbead that is near the pipette tip in Y-axis and closest to the tip in the X-axis, is chose as the microbead of interest, Fig. 11(d) shows the position of the target microbead.

The errors of the micropipette tip detection and the target microbead tracking are within 1pixel, and the sampling time is 100ms. The visual detection with high accuracy and speed provides effective feedback for the controller.

2) Experimental Results of Controller: In the experiments, the microbeads with two typical sizes $15\mu m$ and $5\mu m$ are aspirated by $\sim 25\mu m$ and $\sim 15\mu m$ micropipette under the mi-

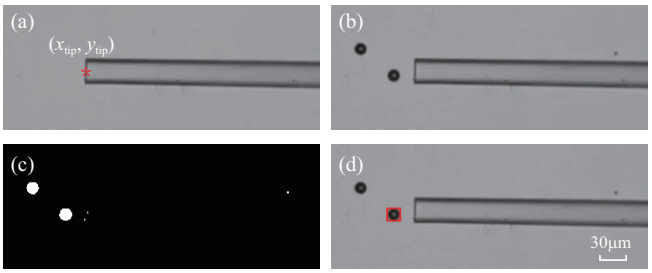

Fig. 11. Microbead tracking. (a) The background image. (b) The current image. (c) The binarized difference image. (d) The tracking results of the target microbead.

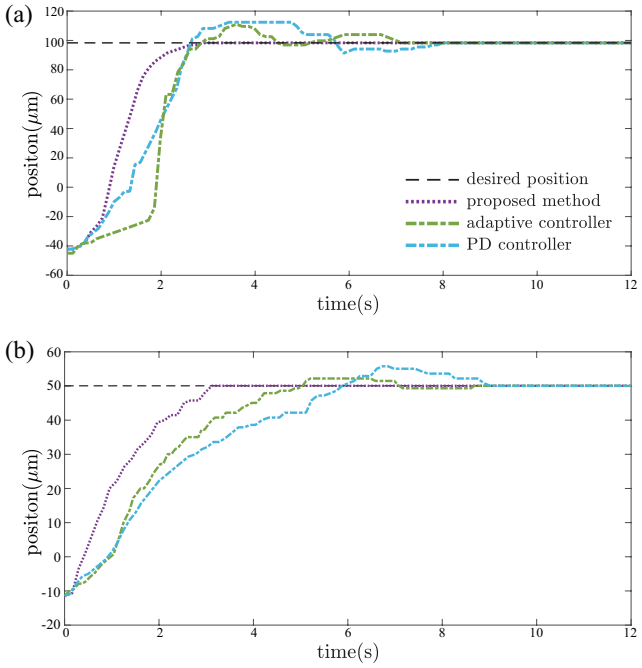

Fig. 12. Experiments results. (a) Microbeads diameter: $15\mu m$; desired value: $98\mu m$. (b) Microbeads diameter: $5\mu m$; desired value: $49\mu m$.

croscope objective of $10\times$ (1pixel = $1.4\mu m$) and $20\times$ (1pixel = $0.7\mu m$), respectively. The position of the micropipette tip is defined as the origin, and the target position is set to 70 pixels from the origin, i.e. $98\mu m$ in $10\times$ objective and $49\mu m$ in $20\times$ objective. The initial position is set to 30pixel ($42\mu m$) for $15\mu m$ beads and 15pixel ($10.5\mu m$) for $5\mu m$ beads.

We place the GLI of the micropipette outside the microscope field of view, so that the movement of the GLI would not affect the visual tracking of the microbeads. The experiment results are shown in Fig. 12. As shown in the purple lines, the position of the microbeads converges to the desired value without overshoot at about 3s by applying the proposed ASMC. In the experiments, the real values of the unknown parameters are different for the microbeads of different sizes. The control system remains stable and the error converges to zero even if the parameters are not precisely estimated, indicating the good robustness of the designed ASMC.

The ASMC is also compared with the model-based adaptive controller [12] and PD controller. As shown in the green lines and the blue lines of Fig. 12, the ASMC converges faster than the adaptive control method (∼8s) and the PD control method (∼10s). The adaptive controller starts to operate after the microbeads enter the pipette. If the velocity of the bead is too high at the micropipette tip, the controller will have not enough time to decelerate the bead, so the bead will go over the target position, leading to overshoot. In this paper, the fluid inside and outside micropipette is analyzed and modeled. The controller compensates for the changes of the system parameters caused by the change of flow velocity, so the overshoot is avoided.

To be noted that, the proposed model and control method are equally applicable to biological cells. Compared to the microbead, the Young's modulus of the cell is smaller, so the cell is easy to be deformed because of the interaction with the pipette wall, when it moves inside the micropipette. However, the inner diameter of the micropipette used in this paper is larger than the cell diameter, and the cell always moves along the center of the pipette during the aspiration process. Therefore, the deformation due to this interaction is extremely small and can be ignored.

V. Conclusion

Cell aspiration with a micropipette is a key technology in cell manipulation. Generally, there is relative motion between the aspirated object and the fluid, resulting in large overshoot even aspiration failure. In this paper, we set up an overall dynamic model of microbead motion inside and outside the micropipette based on CFD. The dynamic model, in which the relative motion of the object and fluid is fully considered, combines microbead motion dynamics, fluid dynamics and pneumatic pump modeling. Based on this model, we design an ASMC for microbead aspiration outside the micropipette and positioning inside the pipette. The controller is proven to achieve asymptotic stability by Lyapunov techniques. Simulations and experiments of the polystyrene microbead aspiration are performed to verify the designed system. The positioning errors of the microbead of different sizes converge to zero without overshoot, revealing the strong robustness of the controller. Compared with the model-based adaptive controller and PD controller, the proposed ASMC demonstrates superior performance due to its fast convergence and non-overshoot. In the future, we will focus on the application of the ASMC to implement cell or sperm aspiration and injection.

Appendix A
Transient Simulation Analysis

In steady-state simulation, the proportion function $h(\cdot)$ is time-independent. We perform transient simulations to further analyze its dynamic performance. In transient simulations, the input pressures are set to *Sine* curves that vary in frequency. When input $u_p(t) = -20+10\sin(\pi t)$, Fig. 13 shows the fluid velocity with time at different locations in the range of [-50, 100]μm along X-axis in the center of the micropipette. The output fluid velocities are *Sine* curves with the same frequency as the input.

When the input pressure has the following form:

$$v_{\mathrm{GLI}}(t) = V_i \sin(\omega t + \phi_1) \tag{25}$$

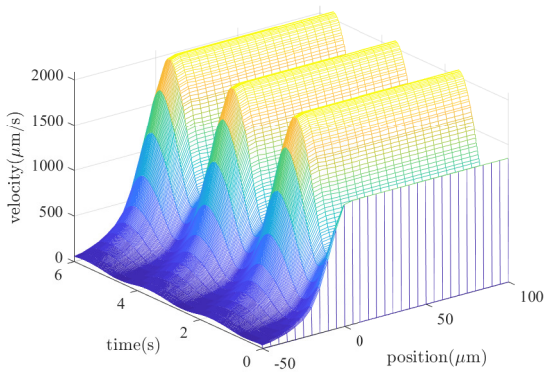

Fig. 13. Transient simulation results.

The fluid velocity along X-axis around the micropipette is:

$$v_f(x,t) = V_f(x)\sin(\omega t + \phi_2) \tag{26}$$

where ϕ_1 and ϕ_2 represent the initial phase of v_{GLI} and v_f, V_i and V_f represent the amplitude.

Simulation results indicate that the maximum difference between ϕ_1 and ϕ_2 is less than 16.5°. The phase difference can be negligible, i.e. $\phi_1 \approx \phi_2$. Therefore, Eq. (13) of $h(\cdot)$ still holds with high-frequency input.

REFERENCES

[1] I. A. Polejaeva, S.-H. Chen, T. D. Vaught, R. L. Page, J. Mullins, S. Ball, Y. Dai, J. Boone, S. Walker, D. L. Ayares *et al.*, "Cloned pigs produced by nuclear transfer from adult somatic cells," *Nature*, vol. 407, no. 6800, pp. 86–90, 2000.

[2] M. Blake, J. Garrisi, G. Tomkin, and J. Cohen, "Sperm deposition site during icsi affects fertilization and development," *Fertility and sterility*, vol. 73, no. 1, pp. 31–37, 2000.

[3] Z. Zhang, X. Wang, J. Liu, C. Dai, and Y. Sun, "Robotic micromanipulation: Fundamentals and applications," *Annual Review of Control, Robotics, and Autonomous Systems*, vol. 2, pp. 181–203, 2019.

[4] J. Zhu, L. Gao, P. Pan, Y. Wang, R. Chen, and C. Ru, "Study of robotic system for automated oocyte manipulation," in *2017 International Conference on Manipulation, Automation and Robotics at Small Scales (MARSS)*. IEEE, 2017, pp. 1–6.

[5] J. Liu, C. Shi, J. Wen, D. Pyne, H. Liu, C. Ru, J. Luo, S. Xie, and Y. Sun, "Automated vitrification of embryos: A robotics approach," *IEEE Robotics & Automation Magazine*, vol. 22, no. 2, pp. 33–40, 2015.

[6] E. Shojaei-Baghini, Y. Zheng, and Y. Sun, "Automated micropipette aspiration of single cells," *Annals of biomedical engineering*, vol. 41, no. 6, pp. 1208–1216, 2013.

[7] A. Shakoor, M. Xie, T. Luo, J. Hou, Y. Shen, J. K. Mills, and D. Sun, "Achieving automated organelle biopsy on small single cells using a cell surgery robotic system," *IEEE Transactions on Biomedical Engineering*, vol. 66, no. 8, pp. 2210–2222, 2018.

[8] Z. Lu, X. Zhang, C. Leung, N. Esfandiari, R. F. Casper, and Y. Sun, "Robotic icsi (intracytoplasmic sperm injection)," *IEEE Transactions on Biomedical Engineering*, vol. 58, no. 7, pp. 2102–2108, 2011.

[9] Y. H. Anis, M. R. Holl, and D. R. Meldrum, "Automated selection and placement of single cells using vision-based feedback control," *IEEE Transactions on Automation Science and Engineering*, vol. 7, no. 3, pp. 598–606, 2010.

[10] X. P. Zhang, C. Leung, Z. Lu, N. Esfandiari, R. F. Casper, and Y. Sun, "Controlled aspiration and positioning of biological cells in a micropipette," *IEEE Transactions on Biomedical Engineering*, vol. 59, no. 4, pp. 1032–1040, 2012.

[11] Z. Zhang, J. Liu, X. Wang, Q. Zhao, C. Zhou, M. Tan, H. Pu, S. Xie, and Y. Sun, "Robotic pick-and-place of multiple embryos for vitrification," *IEEE Robotics and Automation Letters*, vol. 2, no. 2, pp. 570–576, 2017.

[12] G. Shan, Z. Zhang, C. Dai, X. Wang, L.-T. Chu, and Y. Sun, "Model-based robotic cell aspiration: Tackling nonlinear dynamics and varying cell sizes," *IEEE Robotics and Automation Letters*, vol. 5, no. 1, pp. 173–178, 2019.

[13] M. Maxey and B. Patel, "Localized force representations for particles sedimenting in stokes flow," *International journal of multiphase flow*, vol. 27, no. 9, pp. 1603–1626, 2001.

[14] J. D. Anderson and J. Wendt, *Computational fluid dynamics*. Springer, 1995, vol. 206.

[15] M. M. A. Bhutta, N. Hayat, M. H. Bashir, A. R. Khan, K. N. Ahmad, and S. Khan, "Cfd applications in various heat exchangers design: A review," *Applied Thermal Engineering*, vol. 32, pp. 1–12, 2012.

[16] N. Aljuwayhel, G. Nellis, and S. Klein, "Parametric and internal study of the vortex tube using a cfd model," *International journal of refrigeration*, vol. 28, no. 3, pp. 442–450, 2005.

[17] N. Pourmahmoud, H. A. Zadeh, O. Moutaby, and A. Bramo, "Cfd analysis of helical nozzles effects on the energy separation in a vortex tube," *Thermal science*, vol. 16, no. 1, pp. 151–166, 2012.

[18] S. Gilani, H. Montazeri, and B. Blocken, "Cfd simulation of stratified indoor environment in displacement ventilation: Validation and sensitivity analysis," *Building and Environment*, vol. 95, pp. 299–313, 2016.

[19] A. Stamou and I. Katsiris, "Verification of a cfd model for indoor airflow and heat transfer," *Building and Environment*, vol. 41, no. 9, pp. 1171–1181, 2006.

[20] F. Plestan, Y. Shtessel, V. Bregeault, and A. Poznyak, "New methodologies for adaptive sliding mode control," *International journal of control*, vol. 83, no. 9, pp. 1907–1919, 2010.

[21] K. D. Young, V. I. Utkin, and U. Ozguner, "A control engineer's guide to sliding mode control," *IEEE transactions on control systems technology*, vol. 7, no. 3, pp. 328–342, 1999.

[22] N. Fischer, R. Kamalapurkar, and W. E. Dixon, "Lasalle-yoshizawa corollaries for nonsmooth systems," *IEEE Transactions on Automatic Control*, vol. 58, no. 9, pp. 2333–2338, 2013.

[23] T. Ariman, M. Turk, and N. Sylvester, "Applications of microcontinuum fluid mechanics," *International Journal of Engineering Science*, vol. 12, no. 4, pp. 273–293, 1974.